ACS APPLIED MATERIALS & INTERFACES

Research Article

www.acsami.org

Flexible Silver Nanowire Meshes for High-Efficiency Microtextured Organic-Silicon Hybrid Photovoltaics

Ting-Gang Chen,[†] Bo-Yu Huang,[†] Hsiao-Wei Liu,[†] Yang-Yue Huang,[†] Huai-Te Pan,[†] Hsin-Fei Meng,[‡] and Peichen Yu*[,†]

[†]Department of Photonics and Institute of Electro-Optical Engineering and [‡]Institute of Physics, National Chiao-Tung University, Hsinchu, Taiwan, R.O.C.

Supporting Information

ABSTRACT: Hybrid organic-silicon heterojunction solar cells promise a significant reduction on fabrication costs by avoiding energy-intensive processes. However, their scalability remains challenging without a low-cost transparent electrode. In this work, we present solution-processed silver-nanowire meshes that uniformly cover the microtextured surface of hybrid heterojunction solar cells to enable efficient carrier collection for large device area. We systematically compare the characteristics and device performance with long and short nanowires with an average length/diameter of 30 μm/115 nm and 15 μm/45 nm, respectively, to those with silver metal grids. A remarkable power conversion efficiency of 10.1% is achieved with a device area of 1 × 1 cm^2 under 100 mW/cm^2 of AM1.5G illumination for the hybrid solar cells employing long wires, which represents an enhancement factor of up to 36.5% compared to the metal grid counterpart. The high-quality nanowire network displays an excellent spatial uniformity of photocurrent generation via distributed nanowire meshes and low dependence on efficient charge transport under a high light-injection condition with increased device area. The capability of silver nanowires as flexible transparent electrodes presents a great opportunity to accelerate the mass deployment of high-efficiency hybrid silicon photovoltaics via simple and rapid soluble processes.

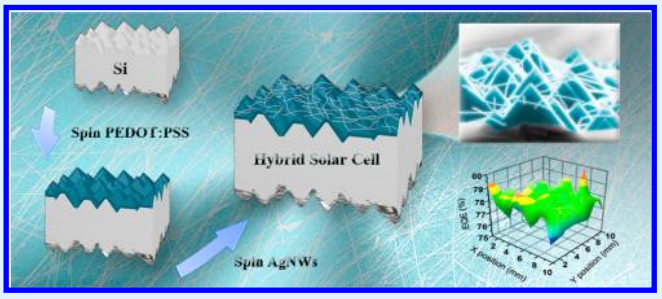

KEYWORDS: *silver nanowire, solution process, conductive polymer, photovoltaics*

Photovoltaic technology is playing an increasingly important role in electricity generation because of rising concerns with petroleum scarcity and green-house gas emissions. Nowadays, crystalline-silicon photovoltaics have a dominant market share for their high efficiency, environmental friendliness, and abundant material supply.[1] However, their energy payback time is still much longer than other thin-film-based technologies,[2] which is largely ascribed to the wafer cost and energy-intensive fabrication processes, such as furnace diffusion (900 °C), electrode cofiring (900 °C), and high-vacuum chemical deposition (400 °C). Consequently, hybrid organic/silicon solar cells have become an attractive approach in which the device combines the advantages of rapid wet-chemical processes with organic materials and wide absorption range with silicon for the heterojunction formation.[3−7] Among the multiple emerging organic materials, hybrid solar cells based on conductive polymer poly(3,4-ethylenedioxy-thiophene):poly-(styrenesulfonate) (PEDOT:PSS) directly spun-cast on planar or nanostructured silicon surfaces exhibit the most promising performance with a power conversion efficiency (PCE) of approximately 10%.[8−12] A validated device model has further projected that an ultimate efficiency of over 20% is possible with the band alignment of PEDOT:PSS and silicon by controlling interface states, surface reflection, and other factors.[13] Nevertheless, efficient carrier collection presents one of the bottlenecks for the scalability of hybrid devices because of the deteriorated series resistance of organic materials in large area. Moreover, the conventional thermally evaporated metal-grid electrodes in a high-vacuum environment also restrain the possibilities of high-throughput production. Therefore a low-cost transparent electrode created through rapid processes is vital to accelerate the mass deployment of hybrid silicon solar cells.

Indium−tin-oxide (ITO) is a high-performance, transparent conducting material widely used in the display and thin-film photovoltaic industries. However, ITO suffers from the long-standing difficulties of indium shortage and brittleness, which further hinder its applications in flexible devices.[14] In the fabrication of hybrid PEDOT:PSS/Si solar cells, the sputtering condition is also likely to damage the underlying polymer and therefore is not preferred.[15,16] Over the past few years, alternatives to ITO have been proposed, including single-walled carbon nanotubes (CNTs) and graphene sheets. The former features high transparency and flexibility but exhibits

Received: September 16, 2012
Accepted: November 20, 2012
Published: November 20, 2012

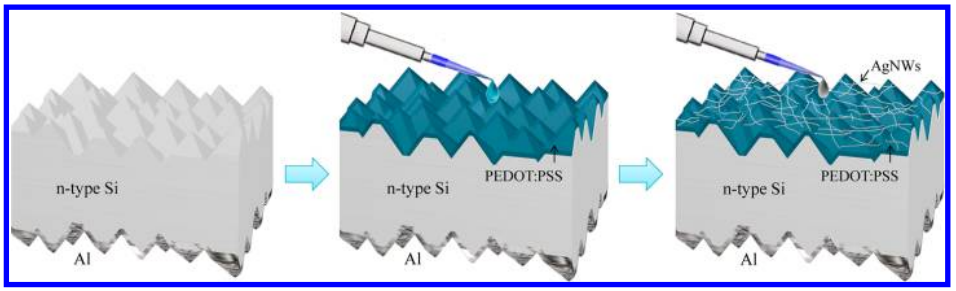

Figure 1. Schematic illustration of the fabrication of a hybrid PEDOT:PSS/Si solar cell with solution-processed heterojunction and AgNW transparent electrodes.

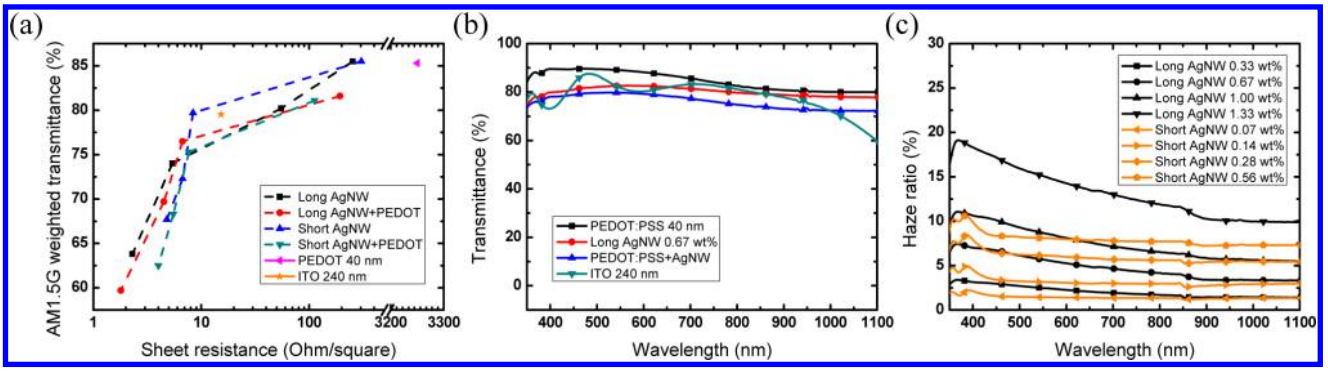

Figure 2. (a) Measured AM1.5G-solar-spectrum-weighted transmittance as a function of the sheet resistance for AgNWs and PEDOT:PSS/AgNW composites prepared with four different suspension concentrations, including the transmittance of glass substrates. (b) Transmittance spectra of the PEDOT:PSS layer, AgNW meshes, both of them, and the referenced ITO coated glass. (c) Haze ratios of long and short AgNWs measured on glass substrates.

relatively low conductivity due to internanotube junction resistance.[17−19] The latter benefits from low material cost, but has the disadvantages of complicated material preparation and transfer processes, leading to a high sheet resistance.[20] Other techniques involving nanoimprint produce high-quality nanoscale electrodes, but the molds cannot be easily applied to textured surfaces.[21] Recently, networks of randomly distributed metal nanowires, such as copper or silver nanowires (AgNWs) have emerged as promising candidates to replace conventional metal grids and ITO thin films because of comparable high transparency and low resistance characteristics in addition to high flexibility in textured and bendable substrates.[22−25] Moreover, synthesis based on the polyol method is a cost-effective approach to obtain size-controlled nanowires,[26,27] which further enables various versatile applications in organic devices.[28−33] In this work, we demonstrate the implementation and characteristics of flexible AgNWs meshes as scalable transparent electrodes for microtextured hybrid PEDOT:PSS/Si solar cells. Long and short AgNWs with different dimensions and suspension concentrations are prepared and both show superior performance over identical cells using thermally evaporated silver grids. A remarkable power conversion efficiency (PCE) of 10.1% is achieved with a device area of 1 × 1 cm^2 under 100 mW/cm^2 of AM1.5G illumination for the hybrid solar cells employing long AgNWs, which represents an enhancement factor of up to 36.5% compared to the metal grid counterpart. Overall, the capability of AgNWs as distributed and flexible transparent electrodes for microtextured PEDOT:PSS/Si hybrid cells enables the simple formation of solution-processed junction and frontal metal electrodes at room temperature and atmospheric ambient, closing the gap in the attainment of high-efficiency, low-cost hybrid silicon photovoltaics.

RESULTS AND DISCUSSION

The fabrication of a solution-processed hybrid PEDOT:PSS/Si heterojunction solar cell with AgNW networks is schematically illustrated in Figure 1. The process starts with an n-type solar-grade monocrystalline silicon wafer, which is surface-textured by an anisotropic wet-etching mechanism employing a potassium hydroxide solution to remove saw damage. This technique is commonly used in the silicon photovoltaic industry for commercial products on 5 in. square wafers. The resulting microscale pyramidal structures, with heights of approximately 2−6 μm, can effectively suppress reflective loss by introducing multiple reflections at the surface and also increase the junction area and conductive paths for photogenerated carriers. The wafer and reference samples are then dipped in dilute hydrofluoric acid to remove the native oxide for the subsequent thermal evaporation of a 100-nm-thick aluminum layer as the rear contact. Next, a highly conductive PEDOT:PSS solution is prepared with appropriate surfactants and additives to achieve a complete surface coverage of PEDOT:PSS on the microtextured surface at a spin rate of 8000 rpm, which was found to be highly correlated to the solar cell performance previously described in.[13] The heterojunction formed by the wide-bandgap p-type PEDOT:PSS and n-type silicon can effectively separate photogenerated excitons, where silicon is the main absorber and the thin PEDOT:PSS acts as a window and hole-conducting layer. Therefore, the device exhibits a very low front surface recombination loss with a working principle analogous to that of Heterojunction with an Intrinsic Thin layer (HIT) solar cells but without the costly

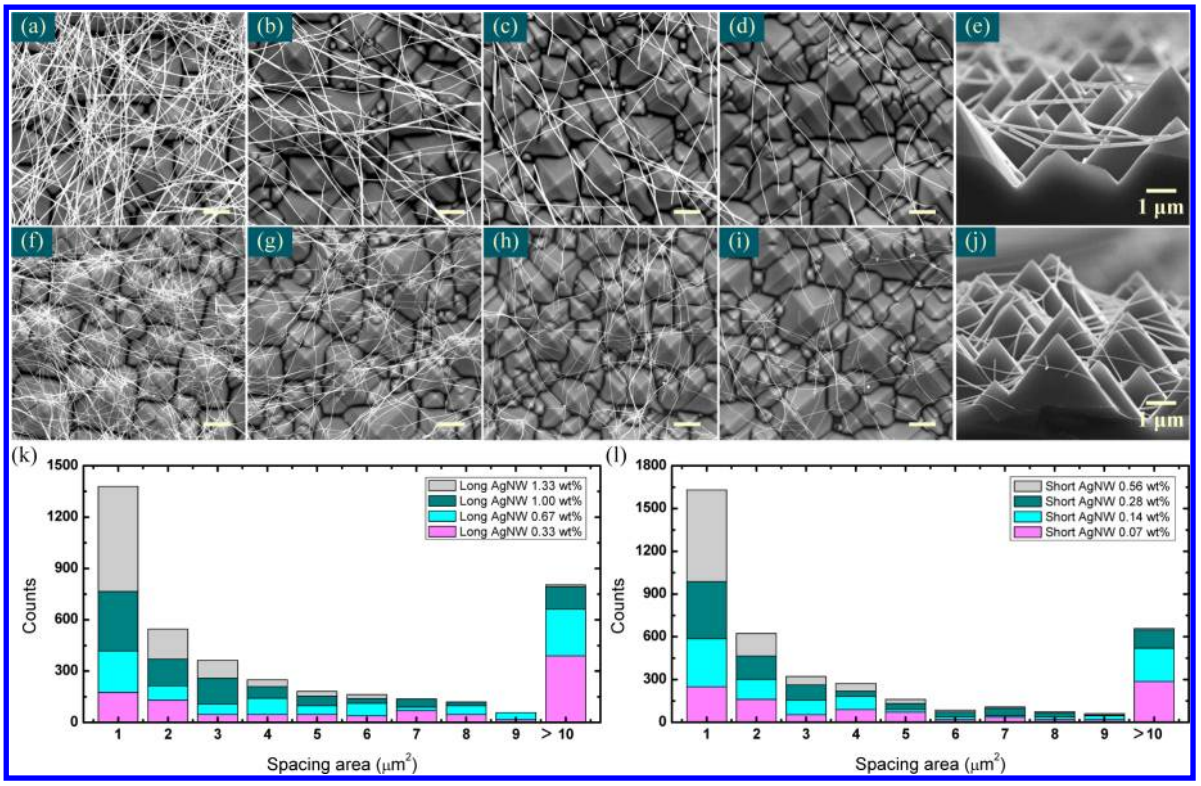

Figure 3. (a–d) SEM images of long AgNWs with concentrations of 1.33, 1.00, 0.67, and 0.33 wt %, respectively, spun-cast on microtextured PEDOT:PSS/silicon solar cells, and (e) the cross-section of b. (f–i) SEM images of short AgNWs with concentrations of 0.56 wt %, 0.28 wt %, 0.14 wt %, and 0.07 wt %, respectively, and (j) the cross-section of g. Unspecified scale bars are 3 μm in length. Histograms of the spacing area distribution for (k) long and (l) short AgNW meshes on micropyramidal surfaces.

high-vacuum processes.[34] Finally, the AgNW meshes are spun-cast onto the microtextured surface, forming distributed metal networks for efficient carrier collection. The finished device consists of a wet-etched micropyramidal n-type silicon substrate with an aluminum rear electrode, a 40-nm-thick PEDOT:PSS layer and AgNW meshes as the frontal electrode. The junction formation and frontal electrode are both achieved by soluble processes, which promise a significant reduction in fabrication costs and also compatibility with current photovoltaic industry techniques. Detailed fabrication processes are described in the Experimental Section.

The properties of AgNW meshes are first investigated by varying the concentration of suspensions and subsequently spin-coating on glass substrates. We prepare long and short AgNWs with lengths/diameters of 30 μm/115 nm and 15 μm/45 nm, respectively, each with four different concentrations: 0.33, 0.67, 1.00, and 1.33 wt % for long wires, and 0.07, 0.14, 0.28, and 0.56 wt %, for short wires using isopropyl alcohol (IPA) as a solvent. The chosen concentrations for long and short AgNWs correspond to similar transparencies on flat glass and roughly equal average spacing areas on microtextured surfaces, to be discussed later. In order to distinctly evaluate the figure of merit of the transmittance spectra for hybrid silicon solar cells, the AM1.5G-solar-spectrum-weighted transmittance is calculated for wavelengths ranging from 300 to 1100 nm using eq 1

$$\left\langle T \right\rangle = \frac{\int_{300\ \mathrm{nm}}^{1100\ \mathrm{nm}} T(\lambda) I_{\mathrm{AM1.5G}}(\lambda) d\lambda}{\int_{300\ \mathrm{nm}}^{1100\ \mathrm{nm}} I_{\mathrm{AM1.5G}}(\lambda) d\lambda} \quad (1)$$

where $T(\lambda)$ denotes the measured transmittance at an incident wavelength λ and $I_{\mathrm{AM1.5G}}$ is the photon flux density of the AM1.5G spectrum. Figure 2a shows the measured weighted transmittance as a function of the corresponding sheet resistance for long and short AgNWs each with the four different concentrations spun-cast on glass substrates. A 40-nm-thick PEDOT:PSS layer and a 240-nm-thick ITO-coated glass are also measured as references. The concentrations of AgNW meshes can be optimized (long, 0.67 wt %; short, 0.14 wt %) to be fairly comparable with the ITO glass with a weighted transmittance of 79.5% and a sheet resistance of 15.3 Ω/□. However, both the transmittance and sheet resistance of AgNW meshes decrease with the increased suspension concentration, which presents a clear trade-off for photovoltaic devices. For hybrid solar cells, the PEDOT:PSS layer itself is very transparent (~85%) but with a poor sheet resistance, which can be as high as 3250 Ω/□, requiring additional metal finger electrodes for effective charge transport. Nevertheless, we find that by incorporating a PEDOT:PSS layer underneath AgNW meshes, the composite reduces the sheet resistance significantly without sacrificing much transmittance, as the soft conductive material provides additional transport paths. The decrease in sheet resistance with the addition of a PEDOT:PSS layer is particularly manifest for sparse AgNW meshes with a sheet resistance larger than 50 Ω/□, whereas in meshes with a sheet resistance below 10 Ω/□, AgNWs dominate the conductivity and the PEDOT:PSS layer makes negligible improvement. These characteristics are very beneficial to hybrid solar cell in which the trade-off between high transmittance and sheet resistance of AgNW meshes can be mitigated by using the AgNW/PEDOT:PSS composite.

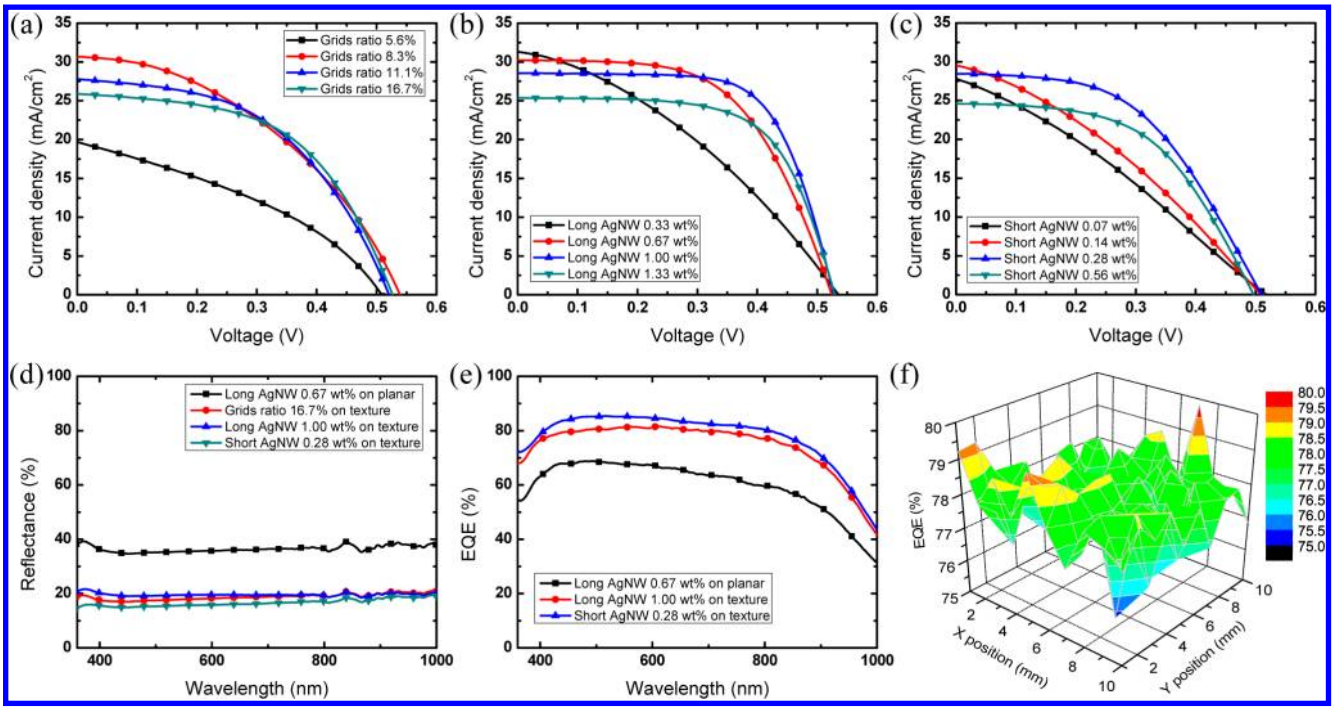

Figure 4. Current density–voltage characteristics of hybrid solar cells with (a) metal grids, (b) long, and (c) short AgNW meshes as frontal electrodes. (d) Measured reflectance and (e) external quantum efficiency (EQE) spectra for best-performing hybrid cells with metal grids and AgNWs meshes. (f) EQE mapping of a 1 × 1 cm^2 hybrid cell with long AgNWs (1.00 wt %) at an incident wavelength of 700 nm, showing an average efficiency of 77.5% with a standard deviation of 0.84%.

Next, the transmittance spectra are plotted in Figure 2b for glass substrates with a 240-nm-thick ITO, 40-nm-PEDOT:PSS layer, long AgNW meshes (0.67 wt %), and the long AgNW/PEDOT:PSS composite. The data indicate that the PEDOT:PSS layer absorbs light for wavelengths above 600 nm and that the AgNWs exhibit reflective losses. Accordingly, the composite PEDOT:PSS layer with AgNW meshes show a final transmittance contributed to the absorption of PEDOT:PSS and reflection of AgNWs and glass substrate. It is noteworthy that the transmittance of AgNW meshes is nearly constant for a broad spectral range, which is very different from the ITO glass because of free carrier absorption at the near-infrared region.[35] Therefore, AgNW meshes are more suitable as transparent electrodes than ITO to enhance the spectral response at the near-infrared to infrared regime. Moreover, AgNW meshes with diameters in the same order as visible-light wavelengths result in scattering of the incident light, which is also advantageous, as it increases the effective optical absorption path for solar cells to improve light harvesting. The scattering capability is generally characterized by a haze ratio, defined as the scattered transmittance divided by the total transmittance, where the scattered component denotes the transmitted light with a scattering angle over 16.7°. Figure 2c shows the spectral response of haze ratios for long and short AgNW meshes spin-coated on a glass substrate with various concentrations. We first observe that the scattering becomes more prominent for high concentrations due to the increased density and layer thickness of AgNW meshes. Moreover, because the total weighted transmittance of long and short wires is comparable at corresponding concentrations (Figure 2a), the long AgNWs appear to scatter light more strongly than the short, particularly in the short wavelength range. This characteristic could be explained by the Mie theory as the scale of long nanowire diameters is closer to the incident wavelengths than the diameters of short wires.[36]

The morphologies of AgNWs on microtextured hybrid cells are investigated next. The AgNW suspensions with various concentrations investigated in Figure 2a are applied to PEDOT:PSS/Si hybrid cells with micropyramidal textures. Figures 3a–d show the scanning electron microscopic (SEM) images for long AgNW meshes on hybrid cells with various concentrations of 1.33, 1.00, 0.67, and 0.33 wt %, respectively. A cross-sectional view of Figure 3b is shown in Figure 3e. Similarly, Figure 3f–i show the short AgNW meshes with concentrations of 0.56, 0.28, 0.14, and 0.07 wt %, respectively, and Figure 3j shows the cross-section of Figure 3g. It can be clearly seen that the density of nanowire meshes is proportional to the concentration of the suspension. Although d and i in Figure 3 present the best optical transparency, the densities of AgNW meshes are too sparse to form a connected network on microtextured surfaces. Moreover, according to the cross-sections, the distribution of short wires with diameters around 45 nm conforms to the micropyramids much better than the long wires with diameters around 115 nm, demonstrating excellent flexibility on textured surfaces. To quantitatively evaluate the network quality from the morphology, we analyzed the distribution of spacing areas enclosed by nanowires in histograms, as shown in k and l in Figure 3 for long and short AgNW meshes, respectively. The total count of each image is normalized to 1000 for comparison. The average spacing area and variance are 20.8 ± 7.8, 10.1 ± 1.4, 5.1 ± 0.3, and 2.3 ± 0.0 μm^2 for long AgNWs, and 19.8 ± 10.3, 9.5 ± 1.7, 5.2 ± 0.4, and 2.4 ± 0.1 μm^2 for short AgNWs (see the Supporting Information, Figure S1). It can be seen that that AgNWs of high concentrations exhibit small and uniform spacing area distributions, while those of low concentrations appear to have

Table 1. Photovoltaic Characteristics of Hybrid Solar Cells Employing Metal Grids and AgNW Meshes As Frontal Electrodes, Including Nanowire Properties, Such As Weighted Reflectance, Shadow Ratio, And Sheet Resistance

samples	V_{oc} (V)	J_{sc} (mA/cm^2)	FF (%)	PCE (%)	series resistance (Ω cm^2)	weighted reflectance (%)	shadow ratio (%)	sheet resistance[a] (Ω/□)
texture, no electrode	0.34	0.43	35.4	0.1	338.6	9.5	0.0	3853.3
planar, long 0.67 wt %	0.55	23.4	54.2	7.0	10.1	36.3	14.0	5.3
planar, short 0.14 wt %	0.54	22.8	48.3	5.9	13.0	35.1	12.7	7.2
grids ratio 5.6%	0.51	19.7	36.6	3.7	9.1	12.3	5.6	
grids ratio 8.3%	0.54	30.7	41.8	6.9	5.4	13.5	8.3	
grids ratio 11.1%	0.52	27.8	48.9	7.1	4.5	15.0	11.1	
grids ratio 16.7%	0.53	25.8	54.2	7.4	4.7	18.6	16.7	
long AgNW 0.33 wt %	0.54	31.3	35.3	5.9	9.6	11.5	4.5	207.4
long AgNW 0.67 wt %	0.52	30.2	56.9	9.0	4.3	16.6	8.9	2.4
long AgNW 1.00 wt %	0.53	28.5	66.9	10.1	3.1	19.6	15.5	1.6
long AgNW 1.33 wt %	0.53	25.4	64.2	8.6	3.7	24.6	27.7	1.7
short AgNW 0.07 wt %	0.52	27.8	30.1	4.3	17.4	10.8	4.1	323.6
short AgNW 0.14 wt %	0.51	29.5	33.6	5.1	12.0	13.2	7.8	31.8
short AgNW 0.28 wt %	0.51	28.5	49.7	7.2	7.2	16.3	14.5	4.5
short AgNW 0.56 wt %	0.50	24.6	53.0	6.5	6.6	20.9	20.3	3.6

[a]Not available for metal grids as they cannot be treated as homogeneous conductive thin films.

various areas larger than 10 μm^2 and uneven spacing distributions with high deviations.

Microtextured PEDOT:PSS/Si hybrid solar cells are fabricated with an area of 1 cm^2 and various frontal electrode configurations including thermally evaporated silver grids, and long/short AgNWs. The silver grids have a fixed width of 100 μm and various spacings, giving rise to shadow ratios of 16.7, 11.1, 8.3, and 5.6%. Alternatively, the long and short AgNWs with the concentrations investigated previously are spun-cast onto the pyramidal surfaces to achieve a distributed charge collection capability. The corresponding current−density−voltage ($J-V$) curves are measured under a simulated AM1.5G one-sun illumination condition and plotted in Figure 4a−c. Planar hybrid solar cells with long and short AgNWs are also employed to compare the characteristics with those of microtextured devices, where the meshes with a concentration of 0.67 and 0.14 wt %, respectively, show a comparable transmittance of 76.5 and 79.7% and a sheet resistance of 6.7 and 8.4 Ω/□ to ITO on a glass substrate (Figure 2a). To elaborate the analysis of fabricated solar cells, we extracted the series resistance from the slope of the light $J-V$ curves at the open-circuit bias point. Also, the surface reflection is measured from the cells using an integrating sphere to capture both, specular and scattered reflection components. We calculate the AM1.5G spectrum weighted reflectance using a similar expression as eq 1. The shadow ratios of AgNW meshes are analyzed based on the SEM images shown in Figure 3. Additionally, the sheet resistance of the PEDOT:PSS/AgNW composite on micropyramidal surfaces is characterized by evaporating a thin SiO_2 insulating layer between the PEDOT:PSS and textured silicon. All the aforementioned information, including photovoltaic characteristics such as the open-circuit voltage (V_{oc}), short circuit current density (J_{sc}), fill factor (FF), and PCE are summarized in Table 1.

As seen in Table 1, a textured PEDOT:PSS/Si hybrid cell without any frontal electrode shows a low J_{sc} (0.43 mA/cm^2) and a low FF (35.4%), which results in a poor PCE (0.1%) because of insufficient carrier conduction. Incorporating a metal grid or nanowire electrode can boost the FF of a hybrid solar cell, which turns to be positively correlated to the grid shadow ratio and nanowire concentrations (Table 1). Because compact grids or distributed nanowires can ensure efficient collection of charge carriers, the conduction improvement is also reflected on the lowered series resistance with dense electrodes as shown in Figure 4a−c. Specifically, the highest FF reaches 54.2 and 53.0% for the silver grids (shadow ratio = 16.7%) and short AgNWs (concentration = 0.56 wt %), respectively, with a device area of 1 cm^2. For long AgNWs, the FF is enhanced even further to 66.9% when using a suspension concentration of 1.00 wt % because of sufficient charge conducting paths under the illumination intensity of 100 mW/cm^2 of the AM1.5G spectrum. On the other hand, the J_{sc} of hybrid solar cells first increases quickly with the grid or nanowire density and then decreases due to electrode obstruction. A J_{sc} of approximately 30 mA/cm^2 or more can be achieved with a moderate grid shadow ratio = 8.3% for specific AgNW concentrations (long. 0.33 wt %; short, 0.14 wt %), but quickly deteriorates with the increased electrode density, which is also reflected on the weighted reflectance. Consequently, the highest PCE of hybrid solar cells occurs at a trade-off between efficient carrier collection and light absorption (see the Supporting Information, Figure S2). A remarkable efficiency of 10.1% is achieved on a 1 × 1 cm^2 hybrid solar cell employing long AgNWs with a concentration of 1.00 wt %, which is far superior to that with metal grids (max. PCE = 7.4%) and with short AgNWs (max. PCE = 7.2%). Moreover, it is noteworthy that the devices with very sparse AgNWs are still capable of generating a high photocurrent, compared with that of the lowest grid ratio, even though the surface reflections from the three electrode configurations are nearly the same (Table 1). This observation highlights the higher effectiveness of distributed electrodes on collecting charge carriers over conventional metal grids. Furthermore, as shown in panels b and c in Figure 4, the short AgNWs show worse FFs than the long wires and yet comparable photocurrent outputs, which is also observed for the planar counterparts (Table 1). The results may be analyzed on the basis of the optical and electrical characteristics, as well as the nanowire morphology on micropyramidal surfaces. First, as the shadow ratios are similar for short and long AgNWs with correspondent concentrations, the short AgNWs reveal higher sheet resistance and lower surface reflectance than the long wires (Table 1 and the Supporting Information, Figure S2).

Therefore, we think that the reduced FF results from two factors. First, the resistivity of AgNWs is dimension-dependent where short AgNWs with smaller diameters exhibit higher resistivity than long AgNWs.[37,38] Second, because of the large surface area of micropyramidal textures (~1.6 times of the planar), the short nanowire network appears to have more intersections, where the wire-to-wire junction resistance may lead to a high sheet resistance compared with the long wires.[39,40] In addition, the comparable photocurrent output can be further examined using the measured reflectance and external quantum efficiency (EQE) spectra. Figure 4d shows the reflectance spectra of the best performing cells with three different electrode configurations, as well as the planar reference with long AgNWs. According to the figure, the planar surface exhibits a high reflective loss (weighted reflectance = 36.3% in Table1), which could be greatly suppressed using surface textures. As expected, long AgNWs show a reduced weighted reflectance of 19.6% from the micropyramidal surface, although still higher than that of short AgNWs (16.3%) and metal grids (18.6%). Nevertheless, the J_{sc} of the long AgNWs coated cell reaches 28.5 mA/cm^2, which is about the same as the short wires and larger than metal grids (25.8 mA/cm^2). Therefore, the long AgNWs show better carrier transport despite high reflection, leading to comparable photocurrent output with short wires. The measured EQE spectra of devices with AgNWs are shown in Figure 4e. We observe that the suppressed reflection due to textured silicon also directly contributes to the EQE enhancement, compared with that of the planar counterpart. Finally, the uniformity of photocurrent generation by means of carrier collection via distributed nanowires can be further analyzed by a spatial EQE mapping tool, which scans the entire 1 × 1 cm^2 cell area with a resolution of 1 mm. Figure 4f shows the quantum efficiency distribution of the 10.1% hybrid solar cell at an incident wavelength of 700 nm. The result shows an average EQE of 77.5% with a standard deviation of 0.84%, in contrast to a 1.45% standard deviation from the best device with metal grids, demonstrating a good uniformity of photocurrent generation using AgNWs as the frontal electrode.

It is worth noting that the integrated photogenerated current based on the EQE spectra of microtextured hybrid cells with AgNWs shown in Figure 4e (long, 30.7 mA/cm^2; short, 32.1 mA/cm^2) does not coincide with the measured J_{sc} from the measured $J-V$ curves (both, 28.5 mA/cm^2). In particular, the device with short AgNWs shows a higher spectral response than with long wires. We think that the discrepancy may arise from the different light bias conditions used in the two characterization systems. To elaborate, the EQE measurement is performed under a low light injection condition, where only a small amount of photogenerated carriers needs to be collected. Therefore, carrier transport within the polymer and nanowire meshes does not suffer from accumulated charges, leading to a space charge limited condition.[41] To investigate further, we apply a bias light during the EQE measurement using a tungsten lamp source with an irradiance of 6.6 mW/cm^2, and define an EQE decrease ratio as a function of the wavelength, calculated by $(EQE_{without\ bias} - EQE_{with\ bias})/EQE_{without\ bias}$, as shown in Figure 5a. Because the definition removes the spectral dependence of the surface reflection and photogenerated carrier distribution of an EQE spectrum, the ratio is nearly wavelength-independent. In other words, the factor represents a figure of merit to evaluate the charge transport capability under the influence of excess carriers with an external light bias. Because

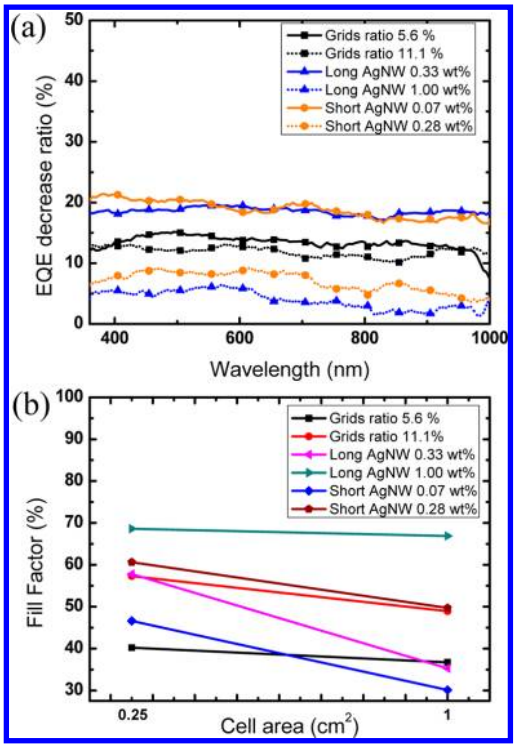

Figure 5. (a) EQE decrease ratios, calculated by $(EQE_{without\ bias} - EQE_{with\ bias})/EQE_{without\ bias}$ for sparse and dense metal grids and AgNW meshes under an external bias light with an irradiance of 6.6 mW/cm^2. (b) Dependence of the fill factor on the cell area varying from 0.25 cm^2 to 1 cm^2 for hybrid cells with metal grids and AgNW electrodes.

the decrease ratio is depicted by the potency of charge transport within the polymer and within the electrode, we can separately analyze the hybrid cells with metal grids and AgNW meshes. First, we observe that the device with large-spacing metal grids (5.6% shadowing) shows a slightly higher EQE decrease ratio than with small-spacing (11.1% shadowing). Although a low decrease ratio basically states that dense grids are advantageous to collect carriers when they are in excess, the marginal difference suggests that charge transport is mainly limited within the PEDOT:PSS layer because of the large grid spacing. On the contrary, the ratios between AgNWs with a high and low suspension concentration can differ by more than 15%, as shown in Figure 5a. First, the sparsest AgNWs meshes for long and short AgNWs show identical EQE decrease ratios, which are both larger than that of the sparsest metal grids. Since the average spacing areas of AgNWs are approximately 20 μm^2, the observation indicates insufficient formations of AgNW networks that worsen the charge transport. With an optimized concentration, the EQE decrease ratio of AgNWs is suppressed down to ~5 and ~8% for the long and short AgNWs, respectively, and the implications could be many-fold. First, the EQE decrease ratios indicate that AgNWs outperform the metal grid for carrier transport due to distributed networks with spacing areas on the order of a few μm^2. Second, charge transport with AgNWs is mainly limited by the conduction within the wire meshes and therefore the long AgNWs (1.00 wt %) exhibit a lower ratio than the short wires (0.28 wt %). As a result, devices with AgNWs exhibit a higher integrated photocurrent than the initial measurement because of limited carrier collection at a high injection condition. Consequently, the short AgNWs may exhibit a higher EQE response than the

long wires. Importantly, the low EQE decrease ratio with the long AgNW meshes further asserts their capability to meet the demands of solar cells used in the AM1.5G illumination condition.

Finally, we investigate the carrier conduction with the three frontal electrode configurations measured for different cell areas. Figure 5b shows the FFs for cells with areas of 0.25 cm^2 and 1 cm^2 employing sparse and dense silver grids and nanowires. Generally, the FFs with all different electrodes encounter a reduction with the increased device area. We can see that the sparse metal grids (5.6% shadowing) show a low FF (40.2%) at a 0.25 cm^2 area, whereas the dense metal grids (11.1% shadowing) improves the FF to 57.3% but then drops to 48.9% for 1 cm^2. The sparse AgNWs show the same attributes as the metal grids, and long AgNW meshes have higher FFs than the short wires at correspondent concentrations. However, the best performing long AgNW meshes with a concentration of 1.00 wt % exhibit only a minor FF decrease from 68.6 to 66.9% by increasing the area, showing great promise to improve carrier conduction for large device area.

CONCLUSION

In conclusion, hybrid PEDOT:PSS/Si solar cells employing typical metal grids and silver nanowires as frontal electrodes are investigated. A power conversion efficiency of 10.1% is achieved in a 1 × 1 cm^2 cell area by means of wet-etched texture surfaces, followed by solution-processed junction and frontal electrodes formation. The external quantum efficiency characterization reveals an excellent spatial uniformity of photocurrent generation via nanowire meshes and suggests a low dependence on efficient charge transport under a high light-injection condition with increased device area. The rapid and simple fabrication processes at room temperature in atmospheric ambient provides a promising cost-effective alternative to conventional silicon photovoltaics.

EXPERIMENTAL SECTION

Hybrid Solar Cell Fabrication. All devices were started from n-type ⟨100⟩ solar-grade monocrystalline wafers with a thickness of 200 μm and a resistivity of 2 Ω cm. The wafers were first immersed in a mixture of potassium hydroxide solution ($KOH:H_2O$ = 1:1) at 80 °C for 40 min to remove any saw damage and texture the surface into micropyramids with heights of ca. 2−6 μm via an anisotropic etching mechanism. No further cleaning steps were taken. The textured and planar samples were subsequently dipped in dilute hydrofluoric acid at a concentration of 1.2% for 20 s to remove the native oxide. After that, a 100-nm-thick aluminum layer was thermally evaporated on the rear surface for ohmic contact. Then, a highly conductive polymer solution was prepared. The mixture consisted of a PEDOT:PSS dispersion (PH1000, Clevios Inc.), 5 wt % dimethyl sulfoxide (DMSO) as a secondary dopant to increase the conductivity, and 0.2 wt % hexaethylene glycol monododecyl ether to act as a surfactant to modify the interface condition between PEDOT:PSS and silicon. Finally, the PEDOS:PSS mixture was directly spun-cast on the silicon surface at 8000 rpm for 120 s followed by thermal annealing at 115 °C for 10 min. All processes were performed at room temperature in atmospheric ambient.

Frontal Electrode Fabrication. All samples with the top PEDOT:PSS layer were processed into cells by adding the frontal electrodes. Conventional silver metal grids with a thickness of 130 nm were thermally evaporated through patterned aluminum foils. The metal grids were designed with a fixed width of 100 μm and varying spacings of 500 μm, 800 μm, 1100 μm, and 1700 μm, corresponding to shadow ratios of 16.7, 11.1, 8.3, and 5.6%, respectively. Two sizes of AgNWs were purchased; the long nanowires were from Seashell Technology (AgNW-115) with lengths of ca. 30 μm and diameters of ca. 115 nm and the short nanowires were from Ke-chuang advanced materials corporation (AW045) with lengths of ca. 15 μm and diameters of ca. 45 nm. The AgNW suspensions were stored in IPA and subsequently diluted down to proper concentrations by the same solvent. A micropipet was used to drop 50 μL of the suspension on the samples and then spun-cast at 2000 rpm for 50 s, followed by heating to 90 °C for 3 min to vaporize any residual solvent. After that, the cells immediately underwent the efficiency measurements.

Optical and Electrical Characterizations. Optical transmittance was carried out using a dual light source and integrating sphere system (U4100, Hitachi Inc.). An InGaAs detector was employed to measure the monochromatic light for a wavelength range of 240 to 2600 nm. A barium sulfate coated integrating sphere with a diameter of 6 cm was used to collect the total transmitted light including specular and scattered components. The scattered transmittance could be recorded by dividing the specular component parallel to the incident light from a circular hole with a diameter of 1.8 cm where the scattered angles of the transmitted light over 16.7° would be categorized as the scattering component. Samples for transmittance and haze ratio measurements were prepared by spin-coating the PEDOT:PSS and AgNW meshes on glass substrates (Eagle 2000, Corning Inc.) and the ITO coated glass was purchased from Sigma-aldrich. Baseline was defined by scanning the blank sample (air), and all the measured data include the 92% transmittance of the glass substrate. The reflectance spectra were measured from complete cells utilizing a custom-built integrating sphere with a diameter of 15 cm to collect the back scattered light in all directions. A 300 W xenon lamp was used as a light source and the photons were analyzed using a spectrometer (SPM-002-ET, Photon-control Inc.). Polished silicon was used for calibration with a spot size of about 1 cm^2. The sheet resistance measurement was performed using standard four-point probes. The sheet resistance in Figure 2 was measured from AgNWs or PEDOT:PSS coated planar glass substrates and the data in Table 1 was measured using planar or textured silicon substrates with a 100-nm-thick SiO_2 layer which was electron-beam evaporated as an insulator between PEDOT:PSS and silicon.

Solar Cell Characterizations. Solar cell performances were characterized using a class A solar simulator (91192A, Newport Inc.) under a standard illumination condition of 100 mW/cm^2 with the AM1.5G spectrum. The temperature of the device under test was controlled at 25 °C by a balanced cooling water and heat plate system. Prior to measurement, the illumination intensity was calibrated using a certified silicon cell from Fraunhofer Inc. A shadow mask with an area of 1 × 1 cm^2 was used to define the illumination area as well as the device area. The areas of finger grids and silver nanowires are included in the device area, but not the bus bars.[42] The solar cells with either AgNWs or metal grid electrodes suffer from efficiency degradation after exposed to air, mainly due to the deteriorated PEDOT:PSS layer. The degradation of AgNWs after spin-coating has not been observed.[43] The EQE system employed a 300 W xenon lamp source with a monochromator for a beam spot size of 1 mm ×3 mm and the signal was detected via a lock-in amplifier (SR830, Standard research system) operated at a chopping frequency of 260 Hz. The intensity was calibrated by a silicon photodetector (818UV, Newport Inc.). To carry out the position-dependent EQE mapping, a labview controlled translation stage was applied under the selected single wavelength of incident light with a resolution of 1 mm. For the light-biased EQE measurement, a 300 W tungsten light source (66984, Newport Inc.) was employed with a 900 nm short-pass filter. The illumination intensity and spectrum were measured by a calibrated spectroradiometer (S-2440, Soma Inc.) with an irradiance of 6.6 mW/cm^2.

ASSOCIATED CONTENT

Supporting Information

The statistical distributions of spacing areas enclosed by AgNWs, and the plots of AM1.5G-spectrum-weighted reflectance, sheet resistance, and power conversion efficiency versus the shadow ratio of various electrode configurations.

This material is available free of charge via the Internet at http://pubs.acs.org/.

AUTHOR INFORMATION

Corresponding Author

*E-mail: yup@faculty.nctu.edu.tw.

Notes

The authors declare no competing financial interest.

ACKNOWLEDGMENTS

The authors thank the National Science Council in Taiwan for financial support under Grant 100-2628-E-009-020-MY3.

REFERENCES

(1) Miles, R. W.; Zoppi, G.; Forbes, I. *Mater. Today* **2007**, *10*, 20−27.
(2) Fthenakis, V. M.; Kim, H. C. *Sol. Energy* **2011**, *85*, 1609−1628.
(3) Zhang, F.; Sun, B.; Song, T.; Zhu, X.; Lee, S. T. *Chem. Mater.* **2011**, *23*, 2084−2090.
(4) Zhang, F.; Han, X.; Lee, S. T.; Sun, B. *J. Mater. Chem.* **2012**, *22*, 5362−5368.
(5) Kalita, G.; Adhikari, S.; Aryal, H. R.; Afre, R.; Soga, T.; Sharon, M.; Koichi, W.; Umeno, M. *J. Phys. D: Appl. Phys.* **2009**, *42*, 115104.
(6) Zhang, F.; Song, T.; Sun, B. *Nanotechnology* **2012**, *23*, 194006.
(7) Shiu, S. C.; Chao, J. J.; Hung, S. C.; Yeh, C. L.; Lin, C. F. *Chem. Mater.* **2010**, *22*, 3108−3113.
(8) Shen, X.; Sun, B.; Liu, D.; Lee, S. T. *J. Am. Chem. Soc.* **2011**, *133*, 19408−19415.
(9) He, L.; Rusli; Jiang, C.; Wang, H.; Lai, D. *IEEE Electron Device Lett.* **2011**, *32*, 1406−1408.
(10) Jeong, S.; Garnett, E. C.; Wang, S.; Yu, Z.; Fan, S.; Brongersma, M. L.; McGehee, M. D.; Cui, Y. *Nano Lett.* **2012**, *12*, 2971−2976.
(11) He, L.; Jiang, C.; Rusli; Lai, D.; Wang, H. *Appl. Phys. Lett.* **2011**, *99*, 021104.
(12) He, L.; Jiang, C.; Wang, H.; Lai, D.; Rusli. *Appl. Phys. Lett.* **2012**, *100*, 073503.
(13) Chen, T. G.; Huang, B. U.; Chen, E. C.; Yu, P.; Meng, H. F. *Appl. Phys. Lett.* **2012**, *101*, 033301.
(14) Zweibel, K. *Sol. Energy Mater. Sol. Cells* **2000**, *63*, 375−386.
(15) Kim, H. K.; Kim, D. G.; Lee, K. S.; Huh, M. S.; Jeong, S. H.; Kim, K. I.; Seong, T. Y. *Appl. Phys. Lett.* **2005**, *86*, 183503.
(16) Gu, G.; Bulović, V.; Burrows, P. E.; Forrest, S. R.; Thompson, M. E. *Appl. Phys. Lett.* **1996**, *68*, 2606−2608.
(17) Wu, Z.; Chen, Z.; Du, X.; Logan, J. M.; Sippel, J.; Nikolou, M.; Kamaras, k.; Reynolds, J. R.; Tanner, D. B.; Hebard, A. F.; Rinzler, A. G. *Science* **2004**, *305*, 1273−1276.
(18) Hu, L.; Hecht, D. S.; Grüner, G. *Nano Lett.* **2004**, *4*, 2513−2517.
(19) Ahmad, K.; Pan, W.; Shi, S. L. *Appl. Phys. Lett.* **2006**, *89*, 133122.
(20) Wang, X.; Zhi, L.; Mllen, K. *Nano Lett.* **2008**, *8*, 323−327.
(21) Kang, M. G.; Kim, M. S.; Kim, J.; Guo, L. J. *Adv. Mater.* **2008**, *20*, 4408−4413.
(22) Rathmell, A. R.; Bergin, S. M.; Hua, Y. L.; Li, Z. Y.; Wiley, B. J. *Adv. Mater.* **2010**, *22*, 3558−3563.
(23) Lee, J. Y.; Connor, S. T.; Cui, Y.; Peumans, P. *Nano Lett.* **2008**, *8*, 689−692.
(24) De, S.; Higgins, T. M.; Lyons, P. E.; Doherty, E. M.; Nirmalraj, P. N.; Blau, W. J.; Boland, J. J.; Coleman, J. N. *ACS Nano* **2009**, *3*, 1767−1774.
(25) Hu, L.; Kim, H. S.; Lee, J. Y.; Peumans, P.; Cui, Y. *ACS Nano* **2010**, *4*, 2955−2963.
(26) Sun, Y.; Gates, B.; Mayers, B.; Xia, Y. *Nano Lett.* **2002**, *2*, 165−168.
(27) Korte, K. E.; Skrabalak, S. E.; Xia, Y. *J. Mater. Chem.* **2008**, *18*, 437−441.
(28) Hardina, B. E.; Gaynora, W.; Dinga, I. K.; Rimb, S. B.; Peumans, P.; McGehee, M. D. *Org. Electron.* **2011**, *12*, 875−879.
(29) Gaynor, W.; Lee, J. Y.; Peumans, P. *ACS Nano* **2010**, *4*, 30−34.
(30) Yang, L.; Zhang, T.; Zhou, H.; Price, S. C.; Wiley, B. J.; You, W. *ACS Appl. Mater. Interfaces* **2011**, *3*, 4075−4084.
(31) Gaynor, W.; Burkhard, G. F.; McGehee, M. D.; Peumans, P. *Adv. Mater.* **2011**, *23*, 2905−2910.
(32) Leem, D.-S.; Edwards, A.; Faist, M.; Nelson, J.; Bradley, D. D. C.; de Mello, J. C. *Adv. Mater.* **2011**, *23*, 4371−4375.
(33) Zhu, R.; Chung, C. H.; Cha, K. C.; Yang, W.; Zheng, Y. B.; Zhou, H.; Song, T. B.; Chen, C. C.; Weiss, P. S.; Li, G.; Yang, Y. *ACS Nano* **2011**, *5*, 9877−9882.
(34) Mishima, T.; Taguchi, M.; Sakata, H.; Maruyama, E. *Sol. Energy Mater. Sol. Cells* **2011**, *95*, 18−21.
(35) Kim, H.; Horwitz, J. S.; Piqúe, A.; Gilmore, C. M.; Chrisey, D. B. *Appl. Phys. A: Mater. Sci. Process.* **1999**, *69*, S447−S450.
(36) Staveren, H. J. V.; Moes, C. J. M.; Marie, J. V.; Prahl, S. A.; Gemert, M. J. C. V. *Appl. Opt.* **1991**, *30*, 4507−4514.
(37) Bid, A.; Bora, A.; Raychaudhuri, A. K. *Phys. Rev. B: Condens. Matter Mater. Phys.* **2006**, *74*, 035426.
(38) Bergin, S. M.; Chen, Y. H.; Rathmell, A. R.; Charbonneau, P.; Li, Z. Y.; Wiley, B. J. *Nanoscale* **2012**, *4*, 1996−2004.
(39) Hecht, D.; Hu, L.; Grüner, G. *Appl. Phys. Lett.* **2006**, *89*, 133112.
(40) Garnett, E. C.; Cai, W.; Cha, J. J.; Mahmood, F.; Connor, S. T.; Christoforo, M. G.; Cui, Y.; McGehee, M. D.; Brongersma, M. L. *Nat. Mater.* **2012**, *11*, 241−9.
(41) Blom, P. W. M.; Mihailetchi, V. D.; Koster, L. J. A.; Markov, D. E. *Adv. Mater.* **2007**, *19*, 1551−1566.
(42) Luque, A.; Hegedus, S. *Handbook of Photovoltaic Science and Engineering*; John Wiley & Sons: London, 2003; p 713.
(43) Liu, C. H.; Yu, X. *Nanoscale Res. Lett.* **2011**, *6*, 75.